

Preparation routes and electrical properties for $\text{Ni}_{0.6}\text{Mn}_{2.4}\text{O}_4$ NTC ceramics

Chengjian Ma¹ · Yunfei Liu¹ · Yinong Lu¹

Received: 9 April 2015 / Accepted: 10 June 2015 / Published online: 17 June 2015
© Springer Science+Business Media New York 2015

Abstract $\text{Ni}_{0.6}\text{Mn}_{2.4}\text{O}_4$ negative temperature coefficient ceramics were prepared by using solid-state coordination reaction and traditional solid-state methods, their structures and properties were characterized by using scanning electron microscopy, powder X-ray diffractometer and temperature dependent resistivity test. For solid-state reaction powders, the calcination temperature necessary for formation of the spinel phase was 1000 °C, which is 300 °C higher than that of solid-state coordination reaction powders. Regardless of preparation routes, the ceramics were crystallized in a single cubic spinel structure when the sintering temperature was lower than or equal to 1150 °C, Mn_3O_4 impurity phase was detected when the sintering temperature raised to 1200 °C. Having higher densities and bigger grain sizes, the solid-state coordination reaction samples had smaller room temperature resistivities and larger $B_{25/50}$ values as compared with those of solid-state samples.

1 Introduction

Manganese-based transition-metal spinel oxide ceramics are widely used as negative temperature coefficient (NTC) thermistor for suppression of in-rush current, temperature measurements, control and compensation [1–4]. In the

spinel structure, the oxygen anions are in a cubic close packed arrangement with cations occupying one-eighth of the tetrahedral interstices (A sites) and one half of the octahedral interstices (B sites) [5]. B constant, which reflects the temperature sensitivity of NTC ceramics, and electrical resistivity ρ are the two main electrical properties of NTC ceramics. Resistivities of these ceramics follow the well know Arrhenius relation: $\rho = \rho_0 \exp(E_a/kT)$, in which ρ is the resistivity, E_a is the activation energy for conduction, k is Boltzmann's constant, and T is the absolute temperature [6].

Nickel manganite is special in manganite-based spinel oxides, because it has a partially inverse structure; $\text{Mn}_v\text{Ni}_{x-v}[\text{Ni}_v\text{Mn}_{3-x-v}]\text{O}_4$, where v is the degree of inversion. The degree of inversion determines both the electrical [7, 8] and magnetic properties [9] of nickel manganite. The inversion parameter is affected by chemical composition [10, 11] and process for preparation [6, 12–14]. Thus it is important to control this parameter. In addition, the sample preparation method affects the oxygen content and the distribution of the cations on the different crystallographic sites, which makes the microstructure and the electrical properties quite different. For example, the resistivity of thin films is different with that of bulk ceramics, which is due to the different densification and grain size [15–18].

So far, however, most of the researches have been focused on adding different metal oxides to tune the room-temperature resistivity and the B value [19–23] and very little attention [24, 25] has been paid to the effect of preparation routes on the microstructure and electrical properties of NTC ceramics. In this study, powders were prepared via the solid-state coordination reaction method and traditional solid-state method. The effect of preparation routes on the microstructure and electrical properties of $\text{Ni}_{0.6}\text{Mn}_{2.4}\text{O}_4$ ceramics was studied.

✉ Yunfei Liu
yfliu@njtech.edu.cn

✉ Yinong Lu
yinonglu@njtech.edu.cn

¹ State Key Laboratory of Materials-Oriented Chemical Engineering, College of Materials Science and Engineering, Nanjing Tech University, No. 5 Xin Mofan Road, Nanjing 210009, China

2 Experimental

As has been described in detail by Ma et al. [14], oxalate precursor $\text{Ni}_{0.6}\text{Mn}_{2.4}(\text{C}_2\text{O}_4)\cdot n\text{H}_2\text{O}$ was prepared by using analytical reagent nickel acetate $\text{Ni}(\text{CH}_3\text{COO})_2\cdot 4\text{H}_2\text{O}$, manganese acetate $\text{Mn}(\text{CH}_3\text{COO})_2\cdot 4\text{H}_2\text{O}$, and oxalic acid $\text{H}_2\text{C}_2\text{O}_4\cdot 2\text{H}_2\text{O}$ as raw materials. For comparison, analytical reagent NiO and MnO_2 powders were weighed in appropriate proportions to fabricate $\text{Ni}_{0.6}\text{Mn}_{2.4}\text{O}_4$ ceramics via traditional solid-state method. The weighed powders were mixed and milled in a planetary mill for 12 h with solvent ethanol. The slurries were dried at 80 °C for 24 h.

The oxalate precursor was calcinated in an alumina crucible at 700 °C for 4 h and the solid-state mixed oxides powder was calcinated at 850, 900, 1000 °C for 2 h, and then the pre-sintered solid-state powder was milled once again for 12 h. Subsequently, the dried powder was pressed with polyvinyl alcohol (PVA) using a hand press to prepare pellets of 1.5 mm-thick and 14 mm in diameter. The green compacts were sintered at 1000–1300 °C for 5 h in air, and then furnace cooled.

To observe the whole reaction process, thermal analysis of oxalate precursor and solid-state oxide mixtures was performed by using thermogravimetric analysis/differential scanning calorimetric analysis (TGA/DSC) (STA 449 F3, NETZSCH, Germany) over 0–1200 °C at a heating rate of 10 °C/min in air. Phase and crystalline structure of the samples were characterized by X-ray diffractometer (XRD) (SmartLab, Rigaku, Japan). The microstructural features of the ceramics were analyzed using Scanning Electron Microscope (SEM) (JSM-6510, JEOL, Japan). For electrical resistance measurements, the two opposite sides of the sintered disks were polished and coated with silver paste, and then heated at 750 °C for 15 min for metalization. The electrical resistance was measured in an oil bath at 25 and 50 °C by a two-probe technique using an PROVA-901 digital multimeter. The B constant was derived according to the formula $B_{25/50} = 3850.16\ln(\rho_{25}/\rho_{50})$, in which ρ_{25} and ρ_{50} are the resistivities at 25 and 50 °C, respectively.

3 Results and discussion

3.1 Analysis of precursors

Figure 1 shows the TGA and DSC results from the oxalate precursors and mixed oxides powders. For the oxalate precursor (Fig. 1a), two intense and sharp peaks of endothermic and exothermic were appeared at 197.7 and 286 °C, which are correspond to the evaporation of crystal water and the decomposition of $\text{Ni}_{0.6}\text{Mn}_{2.4}(\text{C}_2\text{O}_4)\cdot n\text{H}_2\text{O}$, respectively. For the mixed oxides powders (Fig. 1b), the

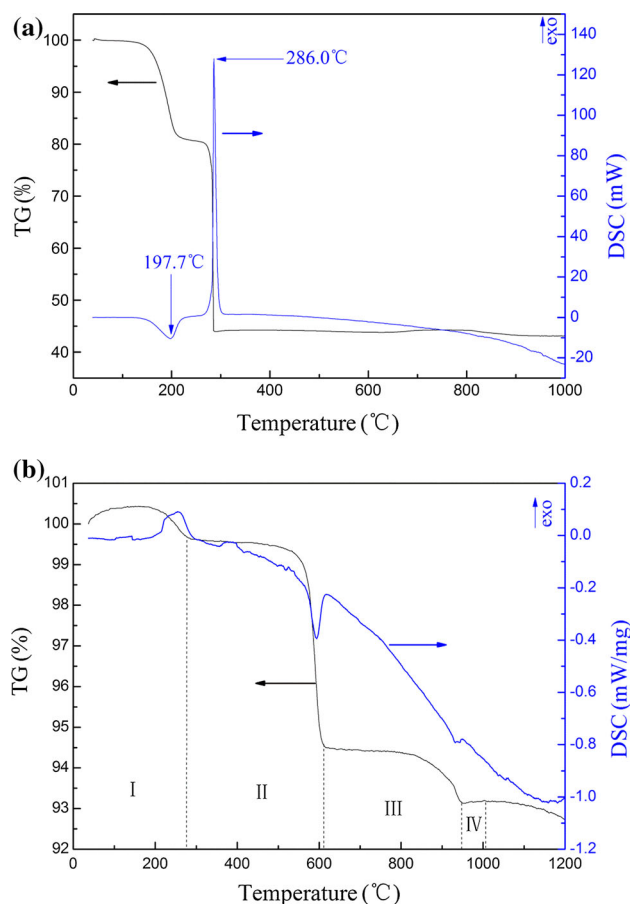


Fig. 1 Simultaneous TGA-DSC curves of the oxalate precursors (a) and mixed oxides powders (b) for $\text{Ni}_{0.6}\text{Mn}_{2.4}\text{O}_4$

weight loss of 0.45 % in region I, accompanied with an exothermic peak at 280 °C, was due to the removal of absorbed water in the samples. Subsequently, several oxido-reduction phenomena were observed. Due to the reduction of Mn^{4+} to Mn^{3+} , one obvious loss of weight was observed in region II [26]. When the temperature was further increased (region III), a weight slightly decreased because of the reduction of the Mn^{3+} to Mn^{2+} [19]. For higher temperatures (region IV), the powders started to gain weight. This was due to the formation of crystalline phases. Finally, for temperatures higher than region IV, we could find a slight weight loss of the powders, which was associated with the loss of excess oxygen, and the stoichiometry of the sample was progressively restored [27].

The phase structure of calcined powders prepared by solid-state coordination reaction method has been discussed previously [14]. While the calcination temperature rose to 700 °C, a single cubic spinel $\text{Ni}_{0.6}\text{Mn}_{2.4}\text{O}_4$ powder was obtained. The XRD patterns of the mixed oxides powders calcined at different temperature range are shown in Fig. 2a–c, respectively. The powders calcined at 850 °C (Fig. 2a) consisted of cubic spinel structure and Mn_2O_3 .

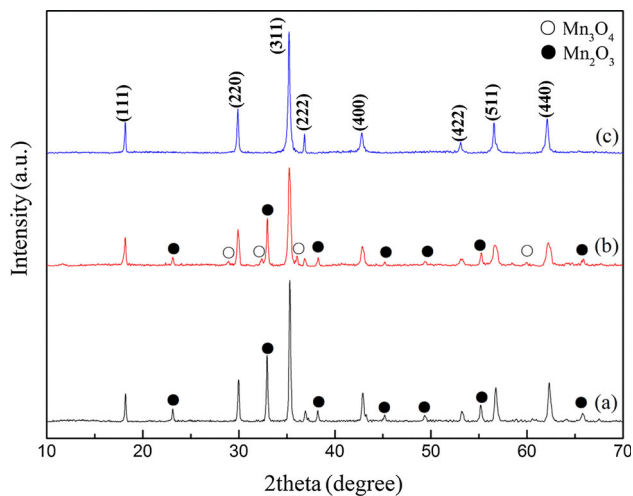


Fig. 2 XRD patterns of powders obtained by calcining metal oxides for 2 h at different temperatures. *a* 850 °C, *b* 900 °C and *c* 1000 °C

Mn_3O_4 was formed in the sample when the calcination temperature rose to 900 °C (Fig. 2b). Further increasing the calcination temperature (Fig. 2c), a single phase with cubic spinel structure was obtained. These results are in good agreement with those of TGA/DSC. Consequently, 1000 °C was used as calcination temperature.

3.2 Analysis of sintered ceramics

Figure 3 exhibits XRD patterns of the $\text{Ni}_{0.6}\text{Mn}_{2.4}\text{O}_4$ ceramics sintered at different temperatures for 5 h. As seen, a single phase with cubic spinel structure was obtained in the samples prepared by both methods while the sintering temperature was lower than or equal to 1150 °C. When the samples were sintered at higher than 1150 °C, Mn_3O_4 was detected in addition to the cubic spinel phase in the samples. The decomposition has been reported previously [14].

The relative densities of the ceramics sintered at different temperatures are shown in Fig. 4. For solid-state coordination reaction samples, the relative density increased rapidly from 84.8 to 97.3 %, and then increased slightly to 98.5 % when the sintering temperature increased from 1000 to 1200 °C. For traditional solid-state samples, it increased from 90.7 to 94.1 % when the sintering temperature increased from 1100 to 1150 °C, and then decreased from 94.1 to 89.2 % when the sintering temperature further increased to 1300 °C. It is noteworthy that the relative density of solid-state coordination reaction samples was much higher than that of traditional solid-state samples when the samples were sintered at the same temperature. It indicates that the sintering activity of powders prepared by solid-state coordination reaction method was higher than that of powders prepared by traditional solid-state method.

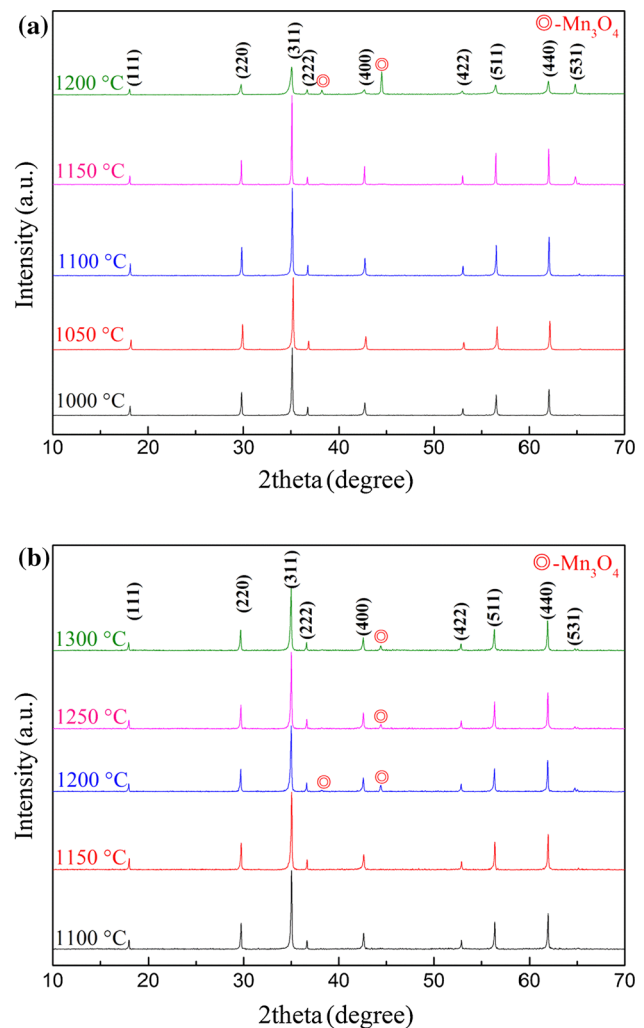


Fig. 3 XRD patterns of the $\text{Ni}_{0.6}\text{Mn}_{2.4}\text{O}_4$ ceramics prepared by using **a** solid-state coordination reaction and **b** traditional solid-state method

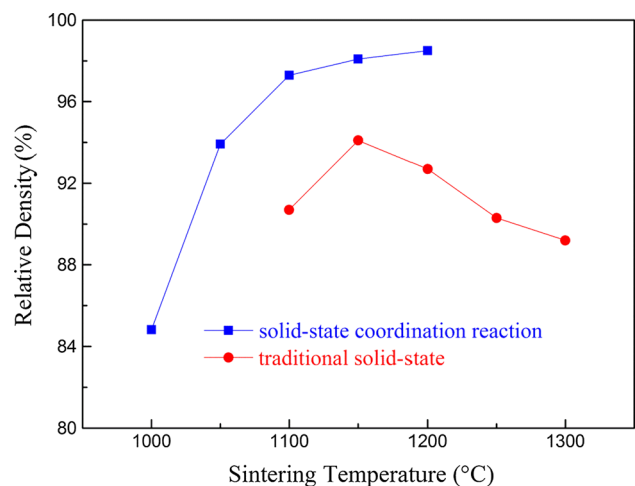


Fig. 4 Relative densities of the ceramics sintered at different temperatures for the solid-state coordination reaction and traditional solid-state $\text{Ni}_{0.6}\text{Mn}_{2.4}\text{O}_4$ samples

Microstructure morphology of the sintered ceramics varies depending on the sintering temperature. SEM images of the ceramics sintered at different temperatures for 5 h are shown in Fig. 5. Results show that the pores content in the ceramics decreased with the increase of sintering temperature for the solid-state coordination reaction samples (Fig. 5a–e). Dense structure could be obtained while the sintering temperature was higher than 1100 °C. However, for traditional solid-state samples, the porosity first decreased and then increased, the minimum value could be obtained when the samples sintered at 1150 °C (Fig. 5f–j). The increase of porosity, along with the pores moved into the grains, was caused by the oversintering [28]. In order to confirm this process, a cross-sectional image of the 1300 °C-sintered traditional solid-state sample was taken and is shown in Fig. 5k. A small amount of pores was found in the grain in addition to a large amount of pores in the grain boundary. A comparison of SEM images of the sintered samples is further evidence demonstrating higher density of the solid-state coordination reaction sample. In addition, it was found that the grain sizes increased with the increase of sintering temperature regardless of preparation routes. The traditional solid-state sample had smaller grain size than that of the solid-state coordination reaction samples.

Room temperature resistivities and $B_{25/50}$ values of the solid-state coordination reaction and traditional solid-state $\text{Ni}_{0.6}\text{Mn}_{2.4}\text{O}_4$ ceramic samples as a function of sintering temperature are shown in Fig. 6. For solid-state coordination reaction samples, the room-temperature resistivity decreased rapidly from 3420 to 2182 Ω cm when the sintering temperature increased from 1000 to 1100 °C, and then increased slightly from 2133 to 2273 Ω cm when the sintering temperature further increased to 1200 °C. The $B_{25/50}$ value increased from 2413 to 3890 K when the sintering temperature increased from 1000 to 1050 °C, and then decreased to 3820 K when the sintering temperature increased to 1200 °C. The $B_{25/50}$ value increased rapidly with increasing sintering temperature, indicating that the ceramic sensitivity improved. For practical applications, a large B value is desirable because the resistivity is more sensitive to variation of temperature, providing more accurate and smaller variations in temperature measurements [14]. However, the room-temperature resistivity decreased from 5291 to 4859 Ω cm when the traditional solid-state samples sintered at 1100 and 1150 °C, then it increased from 4859 to 5020 Ω cm when the sintering temperature further increased to 1300 °C. Small changes had taken place for $B_{25/50}$ value since the sintering temperature changed. The maximum and minimum were 3767 and 3601 K, respectively. It is quite clear that resistivities of the traditional solid-state samples were much larger than those of the solid-state coordination reaction samples and

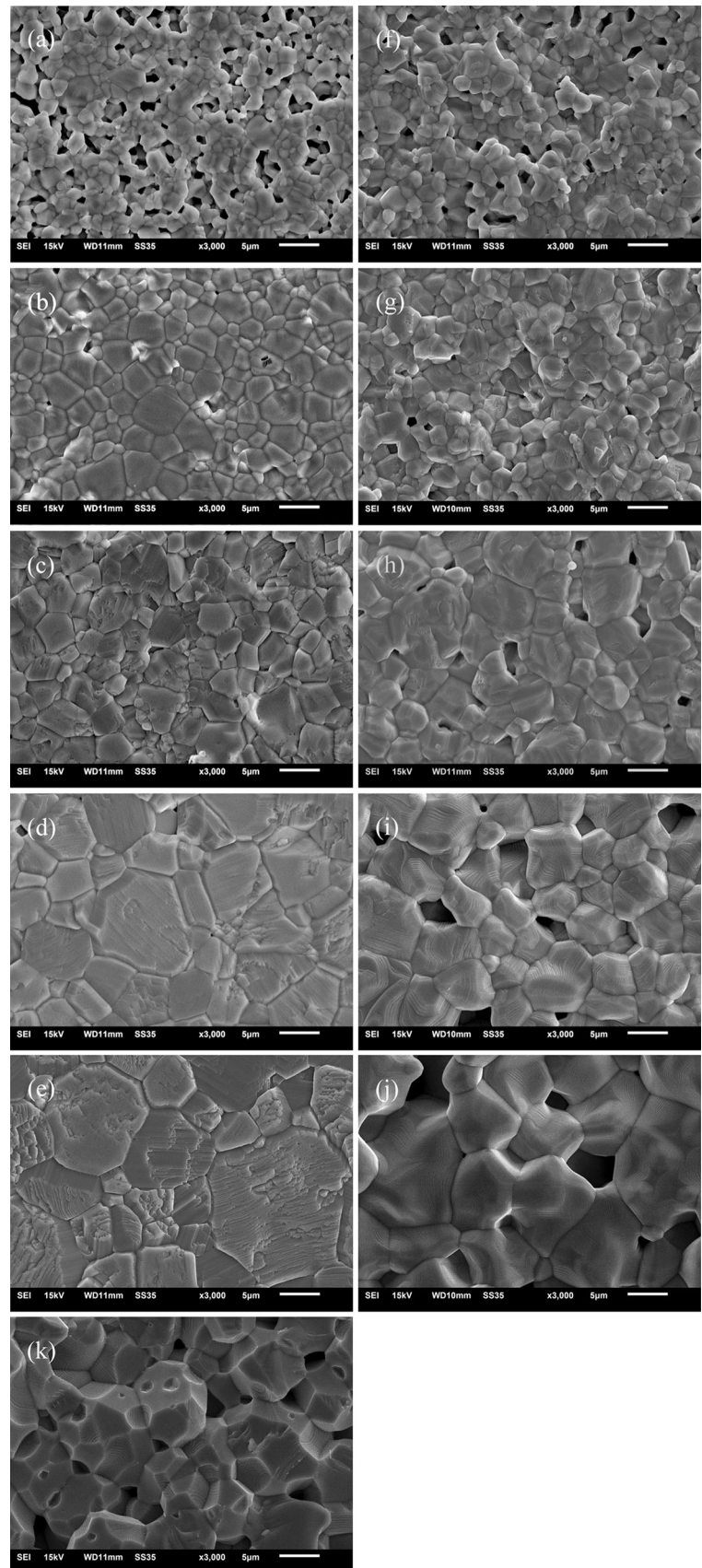
other Mn–Ni–O based samples [23]. The $B_{25/50}$ values of the traditional solid-state samples were smaller than those of the solid-state coordination reaction samples.

As previously reported [29], the total resistance consists of bulk resistance, grain boundary resistance and electrode resistance. The electrical conductivity is satisfactorily described by a phonon assisted hopping of charge carriers between Mn^{3+} and Mn^{4+} on octahedral sites of spinel structure induced by lattice vibrations [30]. In this paper, we believe that the chemical composition of all $\text{Ni}_{0.6}\text{Mn}_{2.4}\text{O}_4$ ceramics is the same, meanwhile, the electrodes were prepared in the same way, so the differences caused by NTC bulk resistance and electrode resistance can be neglected. For solid-state coordination reaction samples, the sample exhibits a larger resistivity when sintered at 1000 °C. This result is caused by the low density and small grain size. Because the sample can be regarded as the NTC particles-air mixture: since air has high resistance, its presence increases the total resistance of the mixture. In addition, the grain size of the sample is small and is over 0.5–2 μm , so there are a lot of grain boundaries in the sample. Grain boundary is the center of the electron scattering, lots of grain boundaries resulting in a high grain boundary resistance [30]. When samples sintered at 1050 °C, the density and grain size increases significantly, as a result, the resistivity decreases. However, when samples sintered at high temperatures, due to the low oxygen partial pressure, reduction reaction would occur [14]. Parts of Mn^{4+} reduces to Mn^{3+} , which gives rise to a decrease in the number of the $\text{Mn}^{3+}/\text{Mn}^{4+}$ couples on octahedral sites, resulting in an increase in resistivity. In addition, the secondary insulative phase, i.e. Mn_3O_4 , also have an influence on the increase of electrical resistivity [12, 31]. For traditional solid-state samples, the total resistivity decreases with the increase of sintering temperature in the range 1100–1150 °C, which is due to the increase of density and grain size. When the sintering temperature is larger than 1150 °C, the significantly decrease in density results in the increase of resistivity. It is also found that the relative density and grain size of the traditional solid-state samples are smaller than those of the solid-state coordination reaction samples. In another words, the contents of porosity and grain boundary of the traditional solid-state samples are bigger than those of the solid-state coordination reaction samples, leading to larger resistivity and smaller $B_{25/50}$ value of the traditional solid-state samples.

4 Conclusions

Preparation route had a great influence on performance of $\text{Ni}_{0.6}\text{Mn}_{2.4}\text{O}_4$ NTC ceramics. Single spinel phase could be achieved when the sintering temperature was lower than or

Fig. 5 SEM images of the ceramics sintered at different temperatures for 5 h for the solid-state coordination reaction (**a** 1000 °C, **b** 1050 °C, **c** 1100 °C, **d** 1150 °C, **e** 1200 °C) and traditional solid-state (**f** 1100 °C, **g** 1150 °C, **h** 1200 °C, **i** 1250 °C, **j** 1300 °C, **k** 1300 °C) $\text{Ni}_{0.6}\text{Mn}_{2.4}\text{O}_4$ samples



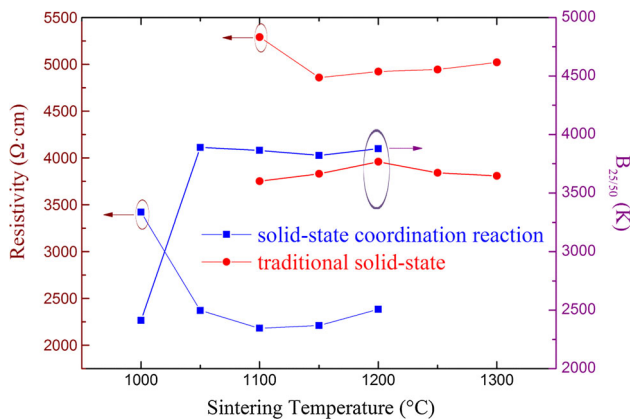


Fig. 6 Room temperature resistivities and $B_{25/50}$ values of the solid-state coordination reaction and traditional solid-state $\text{Ni}_{0.6}\text{Mn}_{2.4}\text{O}_4$ samples

equal to 1150 °C, such phenomenon was detected in both samples prepared by solid-state coordination reaction and traditional solid-state method. Compared with samples prepared by using traditional solid-state method, the $\text{Ni}_{0.6}\text{Mn}_{2.4}\text{O}_4$ ceramics prepared by using solid-state coordination reaction method had higher density and bigger grain sizes. The higher density solid-state coordination reaction samples had smaller grain sizes and fewer grain boundaries, which results in lower room temperature resistivity and higher $B_{25/50}$ value. Thus, solid-state coordination reaction method is an effective route to prepare low room temperature resistivity ceramics, and traditional solid-state method is a simple route to prepare high room temperature resistivity ceramics.

Acknowledgments This work was supported by Major Program for the Natural Scientific Research of Jiangsu Higher Education Institutions (12KJA430002) and Program for Changjiang Scholars and Innovative Research Team in University (PCSIRT), IRT1146. And the authors acknowledge the financial support from Priority Academic Program Development (PAPD) of Jiangsu Higher Education Institutions.

References

1. A. Veres, J. Noudem, O. Perez, S. Fourrez, G. Bailleul, *Solid State Ion.* **178**, 423–428 (2007)
2. K. Park, J.K. Lee, J.G. Kim, S. Nahm, *J. Alloys Compd.* **437**, 211–214 (2007)
3. A. Feteira, *J. Am. Ceram. Soc.* **92**, 967–983 (2009)
4. W. Luo, H.M. Yao, P.H. Yang, C.S. Chen, *J. Am. Ceram. Soc.* **92**, 2682–2686 (2009)
5. K.E. Sickafus, J.M. Wills, N.W. Grimes, *J. Am. Ceram. Soc.* **82**, 3279–3292 (1999)
6. S. Fritsch, J. Sarrias, M. Brieu, J.J. Couderc, J.L. Baudour, E. Snoeck, A. Rousset, *Solid State Ion.* **109**, 229–237 (1998)
7. A. Feltz, W. Polzl, *J. Eur. Ceram. Soc.* **20**, 2353–2366 (2000)
8. R.J.A.E.G. Larson, D.G. Wickham, *J. Phys. Chem. Solids* **23**, 1771–1781 (1962)
9. D.G. Wickham, *J. Inorg. Nucl. Chem.* **26**, 1369–1377 (1964)
10. B. Gillot, J.L. Baudour, F. Bouree, R. Metz, R. Legros, A. Rousset, *Solid State Ion.* **58**, 155–161 (1992)
11. C. Zhao, Y. Zhao, Y. Wang, *Solid State Commun.* **152**, 593–595 (2012)
12. O. Bodak, L. Akselrud, P. Demchenko, B. Kotur, O. Mrooz, I. Hadzaman, O. Shpotyuk, F. Aldinger, H. Seifert, S. Volkov, V. Pekhnyo, *J. Alloys Compd.* **347**, 14–23 (2002)
13. Z. Wang, C. Zhao, P. Yang, L. Winnubst, C. Chen, *Solid State Ion.* **177**, 2191–2194 (2006)
14. C. Ma, Y. Liu, Y. Lu, H. Gao, H. Qian, J. Ding, *J. Mater. Sci. Mater. Electron.* **24**, 5183–5188 (2013)
15. R.N. Jadhav, S.N. Mathad, V. Puri, *Ceram. Int.* **38**, 5181–5188 (2012)
16. R.N. Jadhav, S.N. Mathad, V. Puri, *Phys. Scr.* **87**, 065801 (2013)
17. J. Ryu, K.Y. Kim, J.J. Choi, B.D. Hahn, W.H. Yoon, B.K. Lee, D.S. Park, C. Park, *J. Am. Ceram. Soc.* **92**, 3084–3087 (2009)
18. H. Gao, C. Ma, B. Sun, *J. Mater. Sci. Mater. Electron.* **25**, 3990–3995 (2014)
19. K. Park, *J. Am. Ceram. Soc.* **88**, 862–866 (2005)
20. K. Park, *J. Eur. Ceram. Soc.* **26**, 909–914 (2006)
21. K. Park, J.K. Lee, *J. Alloys Compd.* **475**, 513–517 (2009)
22. Z. Wang, Z. Li, Y. Zhang, R. Zhang, P. Qin, C. Chen, L. Winnubst, *Ceram. Int.* **40**, 4875–4878 (2014)
23. K. Park, D.Y. Bang, J.G. Kim, J.Y. Kim, C.H. Lee, B.H. Choi, *J. Korean Phys. Soc.* **41**, 251–256 (2002)
24. A. Feltz, J. Toepfer, F. Schirmeister, *J. Eur. Ceram. Soc.* **9**, 187–191 (1992)
25. D.F. Li, S.X. Zhao, K. Xiong, H.Q. Bao, C.W. Nan, *J. Alloys Compd.* **582**, 283–288 (2014)
26. E.R. Stobbe, B.A. de Boer, J.W. Geus, *Catal. Today* **47**, 161–167 (1999)
27. K. Park, S.J. Kim, J.G. Kim, S. Nahm, *J. Eur. Ceram. Soc.* **27**, 2009–2016 (2007)
28. S. Golestani-Fard, S. Azimi, K.J.D. Mackenzie, *J. Mater. Sci.* **22**, 2847–2851 (1987)
29. H. Zhang, A. Chang, C. Peng, *Microelectron. Eng.* **88**, 2934–2940 (2011)
30. K. Park, S.J. Kim, *J. Mater. Sci. Mater. Electron.* **15**, 359–362 (2004)
31. M.N. Muralidharan, E.K. Sunny, K.R. Dayas, A. Seema, K.R. Resmi, *J. Alloys Compd.* **38**, 9363–9371 (2011)